JOURNAL OF Materials CHEMISTRY

Synthesis of lithium-rich $Li_xMn_2O_4$ spinels by lithiation and heat-treatment of defective spinels

Xiaojing Yang,*[a] Weiping Tang,[b] Zonghuai Liu,[a] Yoji Makita[a] and Kenta Ooi*[a]

[a]*Marine Resources and Environment Research Institute, National Institute of Advanced Industrial Science and Technology, 2217-14 Hayashi-cho, Takamatsu 761-0395, Japan. E-mail: xiaojing-yang@aist.go.jp, k-ooi@aist.go.jp*
[b]*Research Institute for Solvothermal Technology, 2217-43 Hayashi-cho, Takamatsu 761-0301, Japan*

Received 17th October 2001, Accepted 17th December 2001
First published as an Advance Article on the web 31st January 2002

Single-phase lithium manganese oxide spinels were synthesized in two steps: (1) the preparation of defective spinel precursors with different Li : Mn ratios through lithium insertion into Li-birnessite manganese oxide in a $LiNO_3$ flux at 400 °C, followed by (2) heat-treatment of the precursors at 750 °C in air. Depending upon the Li : Mn ratio, the precursors yielded three types of single-phase spinels: a lithium-deficient type with lithium and oxygen deficiencies, stoichiometric $LiMn_2O_4$, and a lithium-rich type with lithium in the 16d-site of space group $Fd\bar{3}m$ but with oxygen deficiency. The electrochemical measurements showed that good rechargeability on cycling between 3–4.3 V could be obtained in all the lithium-rich spinels $Li[Li_xMn_{2-x}]O_{4-\delta}$, where $0 < x < 0.33$ and $\delta < 0.2$.

Introduction

Spinel $LiMn_2O_4$ and its derivatives are considered to be promising cathode materials for lithium secondary batteries because of their cost performance, nontoxicity and relative stability at high temperature compared with other cathode materials.[1–4] However, significant capacity fading and poor cyclability are shown by $LiMn_2O_4$. This capacity loss, although not well understood, has been attributed to Jahn–Teller cooperative distortion[1] of the $Mn^{3+}O_6$ octahedra,[5,6] the disproportionation reaction of Mn^{3+},[3] and Mn ion dissolution into electrolytic solutions.[4,7] Consequently, the capacity loss is being addressed by exploring various alternatives[2,7–13] to the conventional solid-state methods, and by doping with various elements[3] which decrease the amounts of Mn^{3+} and stabilize the cubic spinel structure with low valence cations (<4). Monovalent Li doping seems to be the best choice since Li provides a larger valence difference relative to Mn than di- or trivalent cations.[14] $Li_xMn_2O_4$ containing excess lithium was found to be more stable and have better rechargeability on cycling.[4,15,16] Furthermore, a high Li : Mn ratio (not less than 0.55) effectively reduces the amount of dissolved Mn.[17]

Tarascon *et al.*[16] indicated that, by the solid-state method with repeated grinding, spinels could be obtained in the range of $0.9 < x < 1.15$ for $Li_xMn_2O_4$, outside the range for Mn_2O_3 and Li_2MnO_3 as the main impurity phases appear for $x < 0.9$ and $x > 1.15$, respectively. Moreover, other methods for the synthesis of $Li_xMn_2O_4$ have been developed. By lithiating MnO_2 polymorphs with LiI solutions to obtain Li_xMnO_2 ($0.4 < x < 0.7$) precursors followed by heating of these precursors, Pistoia *et al.*[18] found that all obtained spinels contained different amounts of Mn_2O_3 and/or Li_2MnO_3, which impaired the electrochemical behaviour. Precursors with a uniform distribution of lithium ions could not restrain formation of the by-products. Xia *et al.*[4] successfully obtained single-phase lithium-rich spinels in the range of $1.0 < x < 1.14$ in $Li_xMn_2O_4$ by using a melt–impregnation method; however, an Li_2MnO_3 phase was also observed for $x > 1.14$. It is comprehensible that the formation of impurity phases of Mn_2O_3 or Li_2MnO_3 depends on precursor properties and synthesizing conditions.

A flux method can produce stoichiometric $LiMn_2O_4$ single crystals,[19–22] which are of benefit to theoretical studies[20] including the mechanism of electrochemical behavior.[21] But it is difficult to obtain a non-stoichiometric single crystal through a flux method. On the other hand, a $LiNO_3$ flux can yield another spinel end member product, $Li_4Mn_5O_{12}$ (or $Li_{1.33}Mn_{1.67}O_4$), at temperatures lower than 500 °C.[19] The reaction between $LiNO_3$ and various MnO_2 polymorphs proceeds through topotactic lithium insertion and oxygen diffusion into manganese oxides.[23] This finding provides a method to insert lithium into manganese oxide. In this work, we investigated the thermal behaviors of the precursors with Li : Mn ratios (<0.8) varying along the MnO_2–$Li_4Mn_5O_{12}$ line of the Li–Mn–O phase diagram.[15] The precursors were prepared through lithium-insertion into Li-birnessite type manganese oxide in a $LiNO_3$ flux. The results showed that this method could supply single-phase $Li_xMn_{2-x}O_{4-\delta}$ spinels with $0 < x < 1.33$, which at the upper end of the range still maintained good rechargeability on cycling at 3–4.3 V.

Experimental

Preparations of precursors

A 200 ml solution of 0.5 M LiOH was mixed with 20 ml 2 M H_2O_2 and then poured into 450 ml 0.3 M $MnCl_2$. After being stirred for 2 hours, the precipitate was centrifuged and washed three times with distilled water until pH = 7–8. The product was dried at 70 °C for 2 days. Li-birnessite manganese oxide (Li-birnessite) was obtained as a very dark brown sample.

Li-birnessite (1 g) was mixed with $LiNO_3$ (15–20 g), and put into a pure alumina crucible (50 ml). A small portion of $LiNO_3$ was placed on the surface of the mixture in the crucible to avoid direct exposure of Li-birnessite particles air at temperatures over 261 °C, the melting point of $LiNO_3$. The crucible was covered with a cap when heated in a muffle furnace. After heating at 400 °C for 6, 12, 24, 36, 48, 60 or 130 hours and air-cooled to room temperature, the products were put into distilled water. The solid was filtered and washed three times, and dried at 70 °C. Finally, purplish-black products were obtained. Analysis of Mn content in the supernatant liquid showed less than 0.007 wt% of Mn dissolution in the flux. The

DOI: 10.1039/b109463g

samples treated in the flux are represented as N*t*h, where *t* is the heating time (hours).

Heat treatment of precursors

Each precursor obtained was put on a dish and heated in a muffle furnace to 750 °C in air. After maintaining at this temperature for 12 hours, the sample was cooled in the furnace to room temperature. All of the heated samples became black. N*t*h-A12h represents the sample heat-treated in air after pre-treatment in a $LiNO_3$ flux for *t* hours.

Physical and chemical analysis

The manganese and lithium contents in the samples were determined by atomic absorption spectrophotometry after dissolving samples in a mixed solution of HCl and H_2O_2. An available oxygen analysis was carried out by the standard oxalic acid method.[24]

The specimens were subjected to thermogravimetric and differential thermal analysis (TG-DTA) (on a MAC Science thermal analyzer, system 001, TG-DTA 2000) at a heating rate of 10 °C min^{-1} in flowing air atmosphere. A Rigaku RINT 2100 powder diffractometer (using Cu-K_α radiation with a graphite monochromator) was used to collect the X-ray diffraction (XRD) data at 30 °C; 2θ ranged from 3 to 70°. Rietveld refinement was carried out using Cerius 2[25] software for some sample data which were taken at 2θ from 10 to 130°, scanning speed 0.2° min^{-1} and sampling step 0.02°.

Raman spectra of the samples were recorded on a Holoprobe 532 Raman system (Kaiser Optical System Inc.) with a microscope attachment at a laser power of 1.0 mW. A JEOL type JSM-890 high-resolution scanning electron microscope was used to observe the morphology of the sample.

Electrochemical measurement

Electrochemical tests were performed to measure quantitatively the electrochemical capacity of the products. The laboratory-scale Li//lithium manganese oxide cells were housed in a Teflon cell apparatus. The electrolyte LIPASTE-EDEC/PF1, obtained from Tomiyama Pure Chemical Industries, Ltd. (Japan), was 1 M $LiPF_6$ in ethylene carbonate (EC)–dimethyl carbonate (DMC) in 1 : 1 volumetric ratio, in which the water content was less than 20 ppm. The separator was polypropylene film. A typical composite cathode consisted of a mixture of lithium manganese oxide powders, acetylene black and colloidal poly(vinylidene fluoride) (PVDF) binder (which was obtained from Kureha Chemical Industry Co., Ltd. (Japan); the concentration of PVDF was 12.0% weight) in a 70 : 20 : 10 weight ratio. When mixing them, 1-methyl-2-pyrrolidone ($CH_3NCOCH_2CH_2CH_2$, Wako Pure Chemical Industries, Ltd., Japan) was used as solvent. The composite was coated on aluminium foil, and heated in a vacuum at 150 °C for 24 hours before inserting in the cell. The cell was assembled in a dry box with argon gas. Galvanostatic charge–discharge cycles were recorded. A current density of 0.2 mA cm^{-2} (about 30–40 mA per milligram lithium manganese oxide) and relaxation time of 10 min between charge and discharge were applied. The charging and discharging were stopped when the closed-circuit voltage reached 4.3 V and 3 V, respectively.

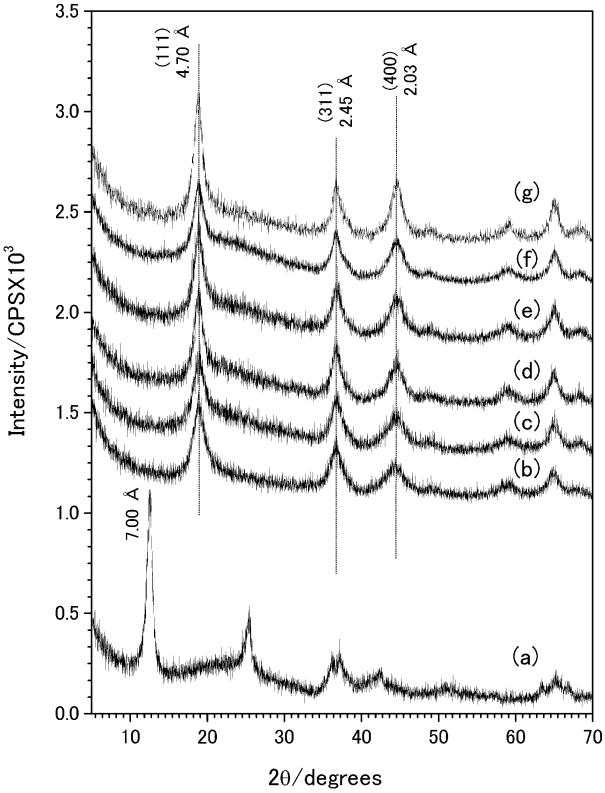

Fig. 1 XRD patterns of (a) Li-Birnessite and N*t*h, which represents the samples heated in a $LiNO_3$ flux for *t* hours, where *t* is (b) 12, (c) 24, (d) 36, (e) 48, (f) 60, and (g) 130.

Results and discussion

Spinel precursor formation in a $LiNO_3$ flux

The XRD patterns and chemical composition for Li-birnessite manganese oxide and its products after heating in a $LiNO_3$ flux are shown in Fig. 1 and Table 1, respectively. The peaks of

Table 1 Composition and structural features

Sample	Analyzed formula	Z_{Mn}	Li/Mn	Li+Mn	Structural feature
Li-birnessite	$Li_{4.26}Mn_{14}O_{27.1}$	3.57	0.30	—	Basal spacing 7.00 Å
N12h	$Li_{0.89}Mn_{1.96}O_4$	3.64	0.45	2.84	Cubic parameter,[a] a_0 = 8.13 Å
N24h	$Li_{0.99}Mn_{1.90}O_4$	3.68	0.52	2.90	
N36h	$Li_{1.01}Mn_{1.87}O_4$	3.74	0.54	2.88	
N48h	$Li_{1.20}Mn_{1.79}O_4$	3.80	0.67	2.99	
N60h	$Li_{1.25}Mn_{1.75}O_4$	3.85	0.71	3.00	
N130h	$Li_{1.37}Mn_{1.67}O_4$	3.97	0.82	3.04	
Li-birnessite-A12h	$Li_{0.69}Mn_{2.22}O_4$	3.30	0.31	2.91	Spinel $LiMn_2O_4$ phase, $a_0 = 8.23_7$ Å, and orthorhombic Mn_2O_3 phase[b], $a = 9.41_1$, $b = 9.37_4$, $c = 9.45_0$
N12h-A12h	$Li_{0.93}Mn_{2.07}O_4$	3.41	0.45	3.01	
N24h-A12h	$Li_{1.02}Mn_{2.00}O_4$	3.49	0.51	3.02	
N36h-A12h	$Li_{1.08}Mn_{1.98}O_4$	3.49	0.54	3.06	
N48h-A12h	$Li_{1.25}Mn_{1.83}O_4$	3.68	0.68	3.08	
N60h-A12h	$Li_{1.29}Mn_{1.80}O_4$	3.73	0.72	3.09	

[a]Average calculated from the *d*-values of (111), (311) and (400) plane. [b]JCPDS card No. 24-0508.

Li-birnessite show a basal spacing of 7.00 Å, while the products show spinel-like patterns. Since the composition of N130h can be regarded as $Li_4Mn_5O_{12}$, the reaction between Li-birnessite and $LiNO_3$ can be written as eqn. (1),

$$5Li_4Mn_{14}O_{27} + 36LiNO_3 \xrightarrow{400^\circ C} 14Li_4Mn_5O_{12} + 36NO_2 + {}^3/_2O_2 \quad (1)$$

This reaction indicates that O^{2-} ions enter the lithium manganese oxide. SEM observation of the Li-birnessite and N130h samples are shown in Fig. 2. The morphology of the birnessite sheet-like particles is retained even in the $Li_4Mn_5O_{12}$ spinel product. This indicates that the transformation from Li-birnessite to spinel proceeds topotactically through a lithium insertion process and an oxygen-diffusion process. Further lithiation of the $Li_4Mn_5O_{12}$ spinel may result in the formation of Li_2MnO_3, as we have observed in other raw material manganese oxides.[23]

A spinel framework quickly forms from Li-birnessite in the N12h sample having the ratio Li/Mn = 0.45 and the mean oxidation state of manganese Z_{Mn} = 3.41, as shown in Fig. 1. The peak positions of the (111), (311) and (400) planes do not show a marked shift but their intensities increase with an increase in the Li : Mn ratio. At the same time, Z_{Mn} also increases with the Li : Mn ratio (Table 1). The fifth column in Table 1 is the summation (Li + Mn) of mole number of cations when the stoichiometric coefficient of oxygen was set to 4. In a spinel phase without defect this value is 3, according to Pollert.[26] The Li+Mn values, 2.8–2.9, of N12h, N24h and N36h suggest some defects exist in their spinel framework. $Li_2Mn_4O_9$ could be regarded as a typical defective spinel with Z_{Mn} = 4, the most likely structure of which is $(Li_{0.89}\square_{0.11})_{8a}[Mn_{1.78}\square_{0.22}]_{16d}O_4$.[27] Since N12h has a higher Li + Mn value (2.84) and lower Li : Mn ratio than $Li_2Mn_4O_9$, it may have oxygen deficiency in addition to the cation deficiencies based on the structural model of $Li_2Mn_4O_9$. Further reaction causes lithium and oxygen ions to enter the defective spinel, leading to a decrease of the deficiencies until Li + Mn = 3. However, during this process the unchanged cubic parameter a_0 (8.13 Å) is smaller than those of $Li_2Mn_4O_9$ (8.174–8.179 Å)[18,27] and $Li_4Mn_5O_{12}$ (8.162, JCPDS card No. 46-0810). This can be explained by considering the orientational distribution of defects or vacancies due to the topotactic reaction. The defects possibly tend to be distributed along the spinel (400) plane, which remained as an interlayer of birnessite; since after accommodating oxygen as well as lithium ions, some remaining spaces can still be detected even in the $Li_4Mn_5O_{12}$ obtained from birnessite.[23] Hence, further lithiation and oxygen diffusion to the initially formed spinel framework do not alter the a_0 value. Because Z_{Mn} monotonously increased with an increase of the Li : Mn molar ratio, the spinels with Li/Mn > 0.5 can be considered to lie in the triangular region of $Li_2Mn_4O_9$–$LiMn_2O_4$–$Li_4Mn_5O_{12}$, rather than along the line of $Li_2Mn_4O_9$–$Li_4Mn_5O_{12}$ in the Li–Mn–O phase diagram.

The Raman spectra of these defective spinels are given in Fig. 3 and compared with reference spectra of spinels $Li_4Mn_5O_{12}$ and $LiMn_2O_4$. The spectrum of $LiMn_2O_4$ shows bands at 623, 581 and 473 and two hardly-resolved bands at around 352 and 300 cm^{-1}. For $LiMn_2O_4$, five modes A_{1g} + E_g + $3F_{2g}$ are predicted to be Raman-active.[28] Ammundsen *et al.*[29] have calculated and observed the lattice vibrational modes. Accordingly, the bands at 623, 581, 473 and 352 can be assigned to the A_{1g}, $F_{2g}(3)$, $F_{2g}(2)$ and $F_{2g}(1)$ vibrations, respectively. The E_g symmetry vibration predicted[29] at 434 cm^{-1} was not observed in the spectrum of the $LiMn_2O_4$ sample. A_{1g} and E_g symmetry vibrations involve only oxide ion displacements, while $F_{2g}(2)$ and $F_{2g}(3)$ are characterized by large oxygen motions and very small Li displacements, and the lowest energy $F_{2g}(1)$ mode derives predominantly from a vibration of the Li sublattice.[29] Julien *et al.*[10,30] suggested that it is also convenient to analyze these spectra in terms of localized vibrations in view of the spinel structure being built of

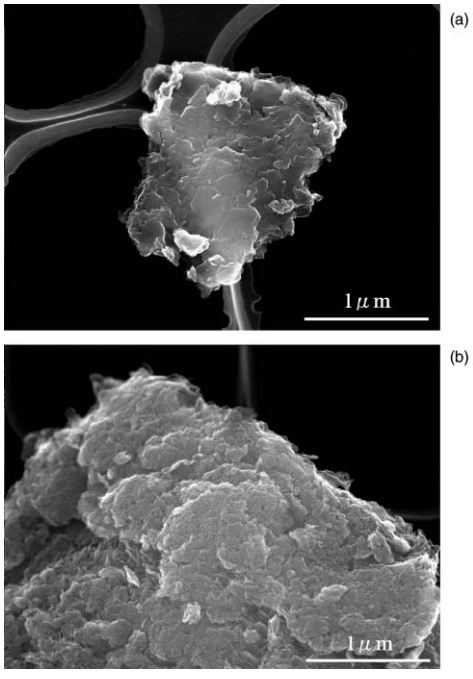

Fig. 2 SEM micrographs of (a) Li-birnessite, and (b) N130h.

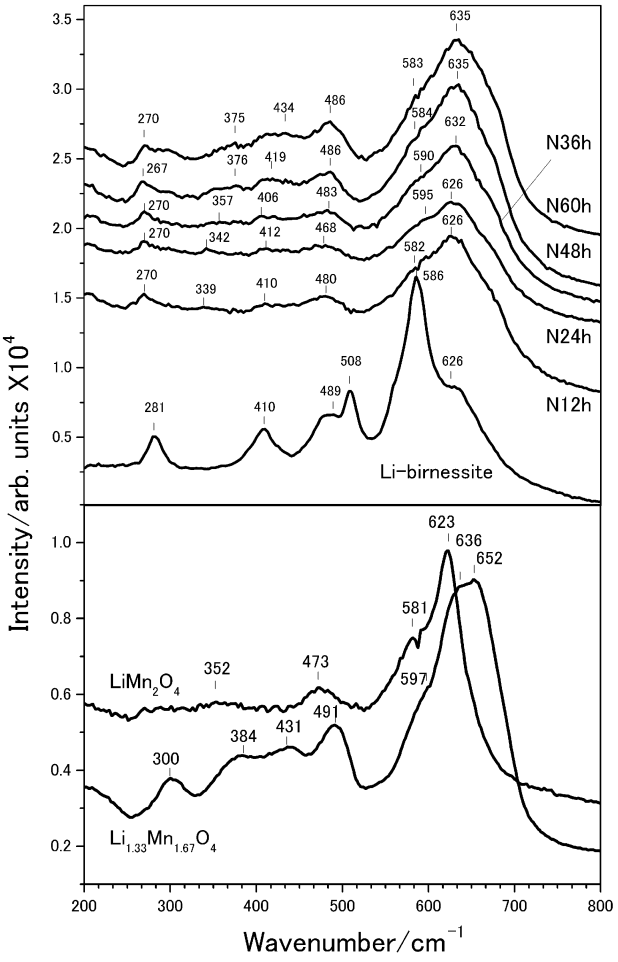

Fig. 3 Raman scattering spectra of Li-birnessite and N*t*h samples with two references, $Li_4Mn_5O_{12}$ prepared by a solid phase reaction method used in the reference[39] and $LiMn_2O_4$ obtained from Aldrich Co. Ltd.

MnO_6 octahedra and LiO_4 tetrahedra. However in the case of $Li_{1.33}Mn_{1.67}O_4$, Li ions occupy one sixth of the 16d sites forming LiO_6 octahedra. The analysis of the spectrum becomes complicated due to cation–anion bond lengths and polyhedral distortion. In the spectrum of $Li_{1.33}Mn_{1.67}O_4$ (Fig. 3), all the bands shift to a high wavenumber, the bands at 384 and 437 cm^{-1} become clear, and another shoulder at 636 cm^{-1} appears. These changes may characterize the existence of LiO_6 octahedra.

The Li-birnessite spectrum is very different from either of the stoichiometric spinels, but the spectra of N*t*h demonstrate that these samples have spinel structures, as shown in the upper part of Fig. 3. For the N*t*h products, the envelope of overlapping bands between 520 and 720 cm^{-1} spectra show that the structure has large polyhedral distortions. The highest band shifts gradually from 626 to 635 cm^{-1} with an increase of lithium and oxygen contents, indicating a probable structural change from that of $LiMn_2O_4$ type to that of $Li_{1.33}Mn_{1.67}O_4$ type. This structural change is also observed at the lower wavenumber region of the spectra, where the relative intensities of the bands at *ca.* 340 and 410 cm^{-1} increase and the bands shift to a high wavenumber. Another band at 270–300 cm^{-1} is observed in the spectra of N*t*h and the reference $Li_{1.33}Mn_{1.67}O_4$ samples, as well as Li-birnessite (at 281 cm^{-1}). It could not be resolved in the spectrum of the $LiMn_2O_4$ sample. But it could not be regarded as a band characteristic of Li ions entering into octahedral sites, because the band at 296 cm^{-1} is associated with the $Li_{0.5}Mn_2O_4$ phase[29] although its structural feature is not clear. Due to lack of calculated data on $Li_{1.33}Mn_{1.67}O_4$, the rich information provided by Raman spectroscopy needs further study.

From the discussion above, it can be concluded that the structural change in the flux occurs as follows: a spinel framework with cations and oxygen defects is formed at Li/Mn < 0.5, further lithiation and oxygen-diffusion reduces the defects until (Li + Mn)/O = 3/4, while Z_{Mn} progressively increases to 4. During the topotactic reaction process, the spinel framework changes from an $LiMn_2O_4$ type to an $Li_{1.33}Mn_{1.67}O_4$ type through lithium entering octahedral sites.

Thermal behavior of the precursors

The TG-DTA curves of the obtained spinel precursors and Li-birnessite are given in Fig. 4. For all the samples, the TG curve shows weight losses before and after 400 °C. After the latter loss, there is a plateau up to 800 °C. For Li-birnessite, the weight losses before 400 °C, accompanied by the endothermic peaks (59, 97 and 181 °C) in the DTA curve, are due to the evaporation of physisorbed water and the dehydration of Li-birnessite. The strong proton bonds in birnessite cause the weight loss up to about 300 °C. For the N*t*h samples, water was adsorbed when the samples were washed after fired in the flux. The composition analysis (Table 1) shows that the Z_{Mn} values of all the samples decrease after being heat-treated at 750 °C for 12 h. The weight loss between 400 and 800 °C is therefore caused by the oxygen release, which corresponds to the reduction of tetravalent manganese, for all the samples.

The XRD patterns for the samples which underwent the heat-treatment at 750 °C for 12 h are given in Fig. 5. Li-birnessite decomposed to a mixture of $LiMn_2O_4$ and Mn_2O_3. The decomposition can be written as eqn (2),

$$Li_4Mn_{14}O_{27} \xrightarrow{>400^{\circ}C} 4LiMn_2O_4 + 3Mn_2O_3 + O_2 \qquad (2)$$

The $LiMn_2O_4$: Mn_2O_3 molar ratio of Li-birnessite-A12h was calculated to be 3/2 from its Z_{Mn} value, 3.3. For N12h-A12h, the Mn_2O_3 phase was not observed in the XRD pattern (Fig. 5(b)), although $LiMn_2O_4$: Mn_2O_3 =82 : 18 was calculated from Z_{Mn} = 3.41. On the other hand, peaks characterized as a monoclinic Li_2MnO_3 phase[31,32] are not

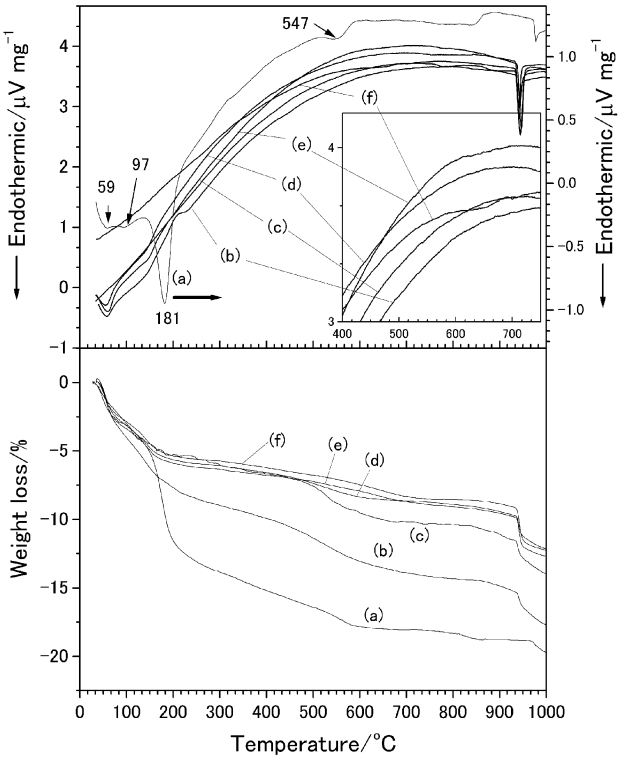

Fig. 4 TG-DTA curves for (a) Li-birnessite, (b) N12h, (c) N24h, (d) N36h, (e) N48h, and (f) N60h.

observed in the XRD patterns, even for the samples of Z_{Mn} > 3.6 and Li/Mn > 0.6, N48h-A12h and N60h-A12h. In other words, heat-treatment of the precursors results in single-phase spinel formation.

The amount of weight loss due to the reduction of Mn^{4+} in

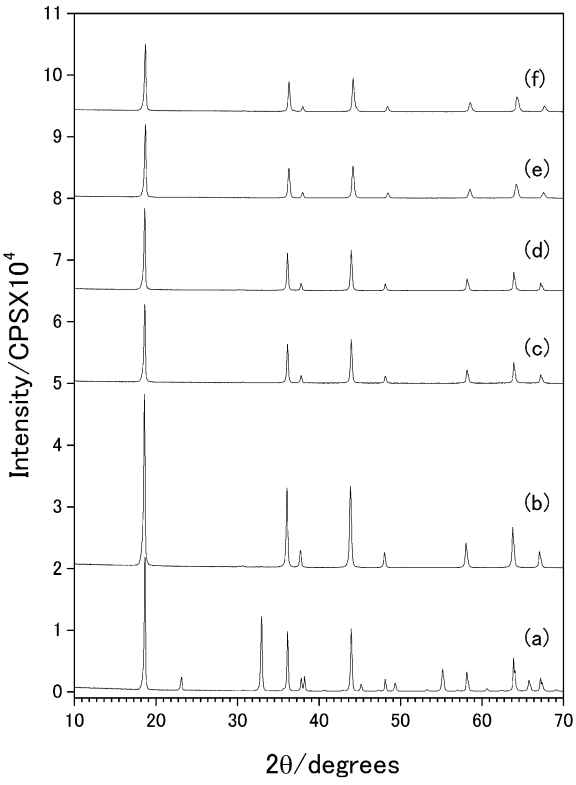

Fig. 5 XRD patterns for the samples (a) Li-birnessite-A12h, and the samples N*t*h-A12h, which represents the sample heat-treated in air for 12 hours after pre-heated in a $LiNO_3$ flux for *t* hours, where *t* is (b) 12, (c) 24, (d) 36, (e) 48, and (f) 60.

the three samples at Li/Mn > 0.5 is much less than those of the other two defective spinel precursors, as shown in the lower part of Fig. 4. In other words, Li ions entering into octahedral sites (Raman result showed) diminish the weight loss of defective spinels. Furthermore, no endothermic peak is observed in the DTA curve related to the greater weight loss of N12h or N24h (Fig. 4(c) or (d)). This is evidence for a secondary phase transition. Broad DTA endothermic peaks appear at around 650 °C corresponding to the lesser weight losses of N48h and N60h respectively (Fig. 4(e) and (f)). The results mean that the weight loss may be brought about by different mechanisms involving the Li/Mn ratio. The compositional change of $Li_2Mn_4O_9$ can represent the change of a $LiMn_2O_4$ type defective spinel as written in eqn. (3) according to de Kock *et al.*,[32]

$$Li_2Mn_4O_9 \xrightarrow{>400^\circ C} 2LiMn_2O_4 + {}^1/_2O_2 \quad (3)$$

Since $Li_4Mn_5O_{12}$ retains its spinel framework when heating up to 750 °C in flowing O_2/air,[33] the reaction can be written as eqn. (4),

$$Li_{1.33}Mn_{1.67}O_4 \xrightarrow{>400^\circ C} Li_{1.33}Mn_{1.67}O_{4-\delta} + {}^\delta/_2O_2 \quad (4)$$

The oxygen loss of eqn. (3) proceeds through a structural rearrangement due to the presence of vacancies, while eqn. (4) indicates only oxygen vacancy formation due to the decrease of Z_{Mn}. Therefore, the weight loss of the spinel precursors with low Li : Mn ratios, not larger than 0.5, may obey eqn. (3). When 0.5 < Li/Mn < 0.8, the weight loss may be caused by eqn. (4), and also (3) because of the presence of cation-vacancies at least at 16d sites. Having a relatively large number of Li ions in octahedral sites, the N48h and N60h weight loss is to a large extent the result of oxygen vacancy formation. The N36h sample has many more cation-vacancies than N48h, so its weight loss is mainly due to structural rearrangement. The absence of a clear endothermic peak for the DTA curve of N48h (Fig. 4(d)) corresponding to the weight loss suggests that this mechanism predominates.

These results clearly indicate that the crystal phase of heat-treated samples depends on the local structure of its spinel precursor. The present defective spinels show a secondary phase transition involving structural rearrangement and/or formation of oxygen vacancies, but not decomposition to mixed phases containing Mn_2O_3 or Li_2MnO_3 impurities, when heat-treated between 400 and 800 °C.

Structure and morphology of heat-treated spinels

The Rietveld refinement results for the samples heat-treated at 750 °C for 12 h are summarized in Table 2. Fig. 6 shows the refinement plots for several representative N*t*h-A12h samples. The low R_{wp} (13–15%) values show that the simulations were successful.[34] The single-phase spinels can be classified into three types according to their structural models in Table 2: (1) when Li/Mn < 0.5, the N12h-A12h spinel has both lithium and oxygen deficiencies. However, it has a_o = 8.245 Å, close to that of the stoichiometric $LiMn_2O_4$ (8.248 Å) of JCPDS card 35-0780; (2) $LiMn_2O_4$, obtained from N24h with Li/Mn close to 0.5; (3) when 0.5 < Li/Mn < 0.8, the spinels have oxygen deficiencies and Li ions occupying 8a and, partially, 16d sites. The lattice parameter of the cubic, a_o, decreased with an increase in the amount of Li in 16d sites.

The Raman spectra for the N*t*h-A12h samples are shown in Fig. 7. The Raman profiles of N24h-A12h and N12h-A12h resemble that of $LiMn_2O_4$ (Fig. 3). As lithium and oxygen increase in the samples, the highest band at 623 cm^{-1} shows a shift to a higher wavenumber, and a new shoulder becomes apparent. The bands at 298, 366 and 422 cm^{-1} gradually strengthen in the low wavenumber range. Finally N60h-A12h exhibits a Raman profile very similar to that of $Li_{1.33}Mn_{1.67}O_4$. These changes show that Li ions enter into octahedral sites with increasing Li : Mn ratio, and the structure changes from $LiMn_2O_4$ type to $Li_{1.33}Mn_{1.67}O_4$ type. This is consistent with the Rietveld refinement results for XRD data. The bands in the low wavenumber range resemble those of corresponding precursors respectively, except for the band at 270 cm^{-1}. But the changes in the envelope between 520 and 720 cm^{-1} indicate a decrease of disorder, *i.e.* the increase of crystallinity. It should be noted that Raman technology is useful for analyzing the local structure of spinels, especially for samples with poor crystallinity, for which it is difficult to apply the Rietveld refinement to the XRD data.

The morphology of N60h-A12h is shown in Fig. 8. The secondary particle is composed of small primary particles, which are uniform in size. Magnification of the lateral surface (Fig. 8(b)) shows that the small particles are plate-shaped. Most of the small plate-shape particles have a clear outline showing morphology different from that of the precursor or Li-birnessite (Fig. 2). Similar morphological changes were

Table 2 Results of Rietveld refinement for XRD data of the N*t*h-A12h samples[a]

Sample	Structure model	Atom	Site	$x = y = z$	Site occupancy	a_o/Å	Refinement parameters	
							R_{wp}(%)	R_p(%)
N12h-A12h	$Li_{0.90}[Mn_2]_{16d}O_{3.86}$	Li	8a	0.125	0.9	8.2453	12.43	9.43
		Mn	16d	0.5	1			
		O	32e	0.2637(1)	0.965			
N24h-A12h	$Li[Mn_2]_{16d}O_4$	Li	8a	0.125	1	8.2294	12.84	9.62
		Mn	16d	0.5	1			
		O	32e	0.2616	1			
N36h-A12h	$Li[Li_{0.06}Mn_{1.94}]_{16d}O_{3.92}$	Li(1)	8a	0.125	1	8.2238	13.95	10.47
		Li(2)	16d	0.5	0.03			
		Mn	16d	0.5	0.97			
		O	32e	0.2636(1)	0.98			
N48h-A12h	$Li[Li_{0.22}Mn_{1.78}]_{16d}O_{3.89}$	Li(1)	8a	0.125	1	8.1873	14.97	10.66
		Li(2)	16d	0.5	0.11			
		Mn	16d	0.5	0.89			
		O	32e	0.2597(5)	0.9725			
N60h-A12h	$Li[Li_{0.25}Mn_{1.75}]_{16d}O_{3.88}$	Li(1)	8a	0.125	1	8.1805	13.56	10.07
		Li(2)	16d	0.5	0.125			
		Mn	16d	0.5	0.875			
		O	32e	0.2612(4)	0.97			

[a]Crystallographic parameters: space group $Fd\bar{3}m$ (227), origin choice 2, in ref. 35.

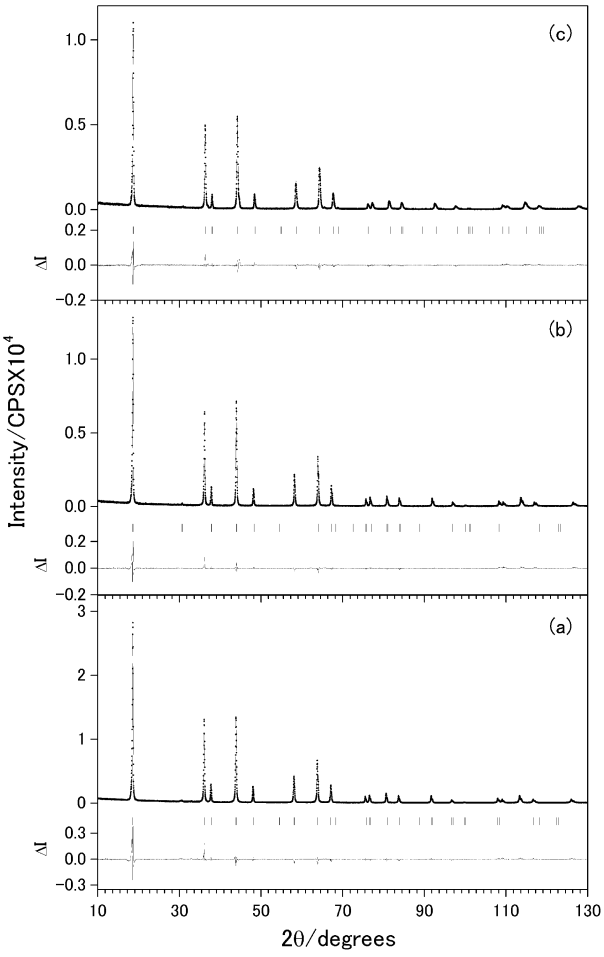

Fig. 6 Rietveld refinement plots for (a) N12h-A12h, (b) N24h-A12h and (c) N60h-A12h. For each sample, the experimental and simulated intensity data (I_e and I_s) are plotted in the above as dotted and solid lines respectively and $\Delta I = I_e - I_s$ below. The tick marks indicate the positions of all possible Bragg reflections from the structural model shown in Table 2.

observed in the other heat-treated samples. The result reveals that the loss of oxygen atoms from the framework as well as the increase of crystallinity by the heat-treatment of the spinel precursors lead macroscopically to the split of the sheet-shaped precursor.

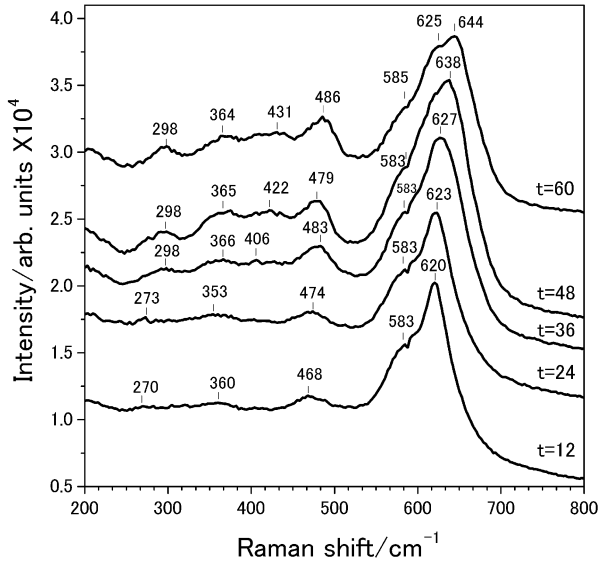

Fig. 7 Raman scattering spectra of the N*t*h-A12h samples.

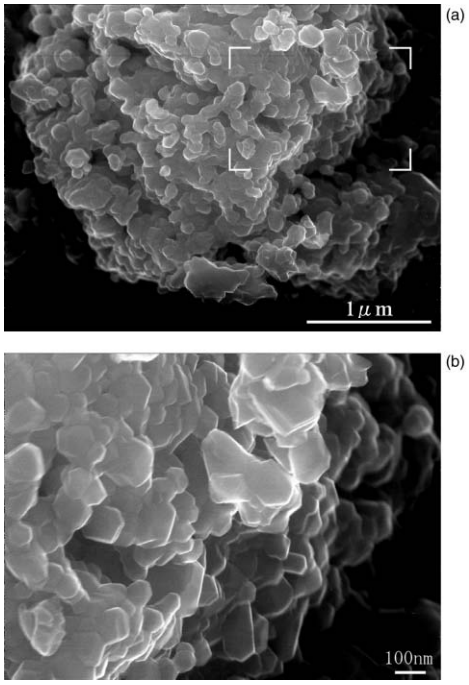

Fig. 8 SEM micrographs of N24h-A12h.

Electrochemical measurement

The first charge–discharge curve and the capacity variation on cycling for the heat-treated samples are given in Figs. 9 and 10, respectively. Samples N12h-A12h, N24h-A12h and Li-birnessite-A12h with Li/Mn $\leqslant$ 0.5 show a two-step charge profile (Fig. 9(b) and (c)) corroborating results in the literatures,[36] and the two-step character is suppressed in the lithium-rich samples, as was also reported by Xia and Yoshio.[37] N36h-A12h does not show a clear two-step profile, and N48h-A12h and N60h-A12h show only a one-step profile. The difference in the charge curves occurs because lithium occupation of 16d sites suppresses the formation of $Li_{0.5}Mn_2O_4$ during lithiation or delithiation of the spinel, confirmed by ^{6}Li NMR results[36] and single-crystal study[22] which show that a local lithium environment appears above 4.1 V in the composition $Li_{0.5}Mn_2O_4$. This suppression effect of lithium ions in the 16d site on the formation of $Li_{0.5}Mn_2O_4$ was earlier found in the delithiation of $LiMn_2O_4$ or lithiation of λ-MnO_2 in aqueous solution.[38,39]

The initial discharge capacity increases with an increase in Li/Mn ratio (N12h-A12h, N24h-A12h), but the rechargeability on cycling is not so good for samples in the range of Li/Mn $<$

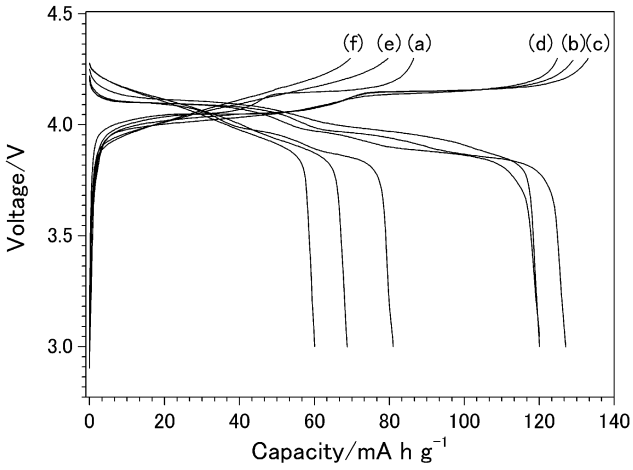

Fig. 9 First charge–discharge curves for (a) Li-birnessite-A12h, and N*t*h-A12h, where *t* is (b) 12, (c) 24, (d) 36, (e) 48, and (f) 60.

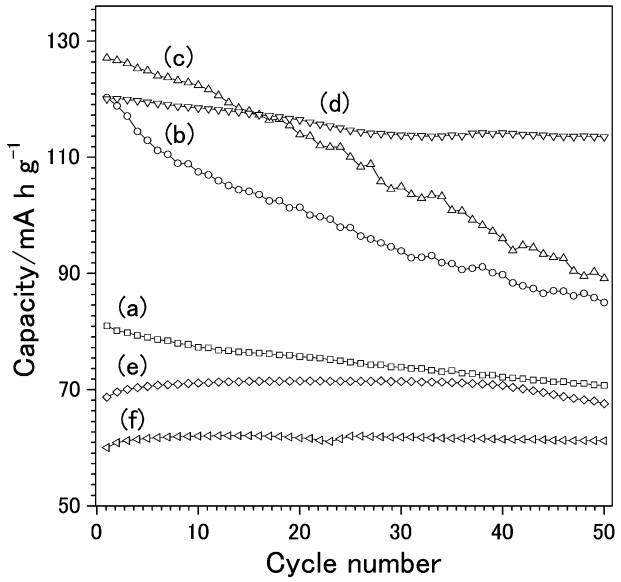

Fig. 10 Variation of the 4 V capacity on cycling for cells using samples of (a) Li-birnessite-A12h, and N*t*h-A12h, where *t* is (b) 12, (c) 24, (d) 36, (e) 48, and (f) 60.

0.5 (Fig. 10). For samples with Li : Mn ratio larger than 0.50, the rechargeability on cycling becomes better as expected[14] and observed for $x < 1.15$ in $Li_xMn_2O_4$,[15,16] while the capacity decreases. Good rechargeability is retained at a much higher x (<1.33), even with the existence of oxygen-deficiency.

Li in 16d-sites suppresses the formation of the $Li_{0.5}Mn_2O_4$ phase during electrochemical delithiation of spinels, and improves the rechargeability over the large range of $0.5 <$ Li/Mn < 0.8. The latter suggest that good rechargeability and large capacity can be obtained by optimizing the Li : Mn ratio in precursors.

Conclusion

A series of plate-form spinels with different Li/Mn ratios were obtained by a topotactic reaction of Li-birnessite in $LiNO_3$ flux at 400 °C. The spinel framework with defects forms prior to Li/Mn < 0.5. Further lithium insertion and oxygen diffusion reduce the defects, and finally bring about the formation of stoichiometric spinel $Li_{1.33}Mn_{1.67}O_4$, accompanied by an increase of the mean oxidation state of manganese.

The defective spinel precursors lose oxygen when heated at 750 °C in air, maintaining the spinel framework without producing Mn_2O_3 or Li_2MnO_3 phases. They yield three kinds of single-phase spinels; with lithium and oxygen deficiencies at Li/Mn < 0.5, $LiMn_2O_4$ at Li/Mn $= 0.5$, and with oxygen deficiency and lithium ions in 16d sites at $0.5 <$ Li/Mn < 0.8. The latter kind of spinels gives good rechargeability on cycling. The sheet-shaped particle of the precursor changes to small uniform plate-like particles.

Raman spectroscopy is a useful method for differentiating the fine structure of cubic spinel structures in which 16d sites are occupied by manganese ions or displaced partially by lithium ions.

References

1 A. Yamada, K. Miura, K. Hinokuma and M. Tanaka, *J. Electrochem. Soc.*, 1995, **142**, 2149.
2 W. Liu, G. C. Farrington, F. Chaput and B. Dunn, *J. Electrochem. Soc*, 1996, **143**, 879.
3 M. M. Thackeray, *J. Am. Ceram. Soc.*, 1999, **82**, 3347.
4 Y. Xia, H. Takeshige, H. Noguchi and M. Yoshio, *J. Power Sources*, 1995, **56**, 61.
5 V. Weightarotti, D. Capsoni, M. Bini, G. Chiodelli, C. B. Azzoni and A. Paleari, *J. Solid State Chem.*, 1997, **131**, 94.
6 A. Yamada, M. Tanaka, K. Tanaka and K. Sekai, *J. Power Sources*, 1999, **81-82**, 73.
7 D. H. Jan, Y. J. Shin and S. M. Oh, *J. Electrochem. Soc.*, 1997, **144**, 3342.
8 T. Soshima, K. Okahara, C. Kiyohara and K. Shizuka, *J. Power Sources*, 2001, **97-98**, 377, and references therein.
9 G. Pistoia, A. Antonini, R. Rosati, C. Bellito and G. M. Ingo, *Chem. Mater.*, 1997, **9**, 1443.
10 C. Julien, S. Ziolkiewicz, M. Lemal and M. Weightot, *J. Mater. Chem.*, 2001, **11**, 1837.
11 Y. K. Sun, I. H. Oh and K. Y. Kim, *Ind. Eng. Chem. Res.*, 1997, **36**, 4839, and references therein.
12 B. Ammundsen, D. J. Jones, J. Roziere and G. R. Burns, *Chem. Mater.*, 1997, **9**, 3236.
13 Q. Feng, K. Yanagisawa and N. Yamasaki, *Chem. Commun.*, 1996, 1607.
14 N. V. Kosova, N. F. Uvarov, E. T. Devyatkina and E. G. Avvakumov, *Solid State Ionics*, 2000, **135**, 107.
15 M. M. Thackeray, A. De Kock, M. H. Rossouw, D. Liles, R. Bittihn and D. Hoge, *J. Electrochem. Soc.*, 1992, **139**, 363.
16 J. M. Tarascon, W. R. McKinnon, F. Coowar, T. N. Bowmer, G. Amatucc and D. Guyomard, *J. Electrochem. Soc.*, 1994, **141**, 1421.
17 K. Nishimura, T. Dousono, M. Kasai, H. Andou, Y. Muranaka and Y. Kozono, *J. Power Sources*, 1999, **81-82**, 420.
18 G. Pistoia, A. Antonini, D. Zane and M. Pasquali, *J. Power Sources*, 1995, **56**, 37.
19 X. Yang, W. Tang, H. Kanoh and K. Ooi, *J. Mater. Chem.*, 1999, **9**, 2683.
20 J. Akimoto, Y. Takahashi, Y. Gotoh and S. Mizuta, *Chem. Mater.*, 2000, **12**, 3246.
21 W. Tang, X. Yang, H. Kanoh and K. Ooi, *Chem. Lett.*, **2001**, 524.
22 H. Bjork, T. Gustafsson and J. O. Thomas, *Eletrochem. Commun.*, 2001, **3**, 187.
23 X. Yang, H. Kanoh, W. Tang and K. Ooi, *J. Mater. Chem.*, 2000, **10**, 1903.
24 Japan Industrial Standard (JIS), 1969, M8233.
25 Cerius2 Modeling Environment, Release 4.0, San Diego, Molecular Simulations Inc., 1999.
26 E. Pollert, *Prog. Cryst. Growth Charact.*, 1984, **9**, 263.
27 P. Strobel, A. Ibarra Palos and M. Anne, *J. Power Sources*, 2001, **97-98**, 381.
28 W. B. White and B. A. De Angles, *Spectrochim. Acta*, 1967, **23A**, 985.
29 B. Ammundsen, G. R. Burns, M. S. Islam, H. Kanoh and J. Roziere, *J. Phys. Chem. B*, 1999, **103**, 5175.
30 C. Julien, E. Haro-Poniatowski, M. A. Camacho-Lopez, L. Escobar-Alarcon and J. Jimenez-Jarquin, *Mater. Sci. Eng.*, 2000, **B72**, 36.
31 C. H. Berg, E. M. Kelder and J. O. Thomas, *J. Mater. Chem.*, 1999, **9**, 427.
32 A. de Kock, M. H. Rossouw, L. A. De Picciotto, M. M. Thackeray, W. I .F. David and R. M. Ibberson, *Mater. Res. Bull.*, 1990, **25**, 657.
33 T. Takada, H. Hayakawa, T. Kumagai and E. Akiba, *J. Solid State Chem.*, 1996, **121**, 79.
34 F. Izumi, *J. Jpn. Crystal. Soc.*, 1985, **27**, 23 (in Japanese).
35 *International Tables for crystallography*, volume A, 2nd revised edition, ed. T. Hahn, D. Reidel Publishing Company, Holland, 1987.
36 Y. J. Lee, R. Wang, S. Mukerjee, J. McBreen and C. P. Grey, *J. Electrochem. Soc.*, 2000, **147**, 803.
37 Y. Xia and M. Yoshio, *J. Electrochem. Soc.*, 1996, **143**, 825.
38 K. Ooi, Y. Miyai, S. Katoh, H. Maeda and M. Abe, *Langmuir*, 1989, **5**, 150.
39 Q. Feng, Y. Miyai, H. Kanoh and K. Ooi, *Langmuir*, 1992, **8**, 1861.